Supporting Information

Baggen et al. 10.1073/pnas.1713284115

SI Materials and Methods

Cell Lines. HAP1 and HAP1 *CMAS*^{KO} cells were obtained from Haplogen GmbH and cultured in Iscove's Modified Dulbecco's Medium (IMDM; Lonza) containing 10% (vol/vol) FCS. HeLa-R19 cells were obtained from G. Belov, University of Maryland, College Park, MD, and cultured in DMEM (Lonza) containing 10% (vol/vol) FCS. Huh7/Lunet/T7 cells were obtained from Ralf Bartenschlager, Heidelberg University Hospital, Heidelberg, and cultured in DMEM containing 10% (vol/vol) FCS. HCE cells were obtained from Kaoru Araki-Sasaki, Hoshigaoka Medical Center, Hoshigaoka, Japan, and cultured in supplemented hormonal epithelial medium, consisting of DMEM and Ham's F-12 nutrient mixture mixed 1:1, supplemented with insulin (5 μg/mL), cholera toxin (0.1 μg/mL), epidermal growth factor (10 ng/mL), DMSO (0.5%), gentamycin (40 μg/mL), and 15% vol/vol FCS. HC0597 were obtained from ATCC (CRL-12658) and were cultured as described previously (1). All cell lines were tested for mycoplasma contamination.

Viruses. CV-A24v strains (110386, 110387, 110388, 110389, 110390, 110391, and 110392) originated from an outbreak in Malaysia in the 2002–2003 period (2) and were obtained from Steve Oberste, Centers for Disease Control and Prevention, Atlanta. EV-D68 Fermon (CA62-1), CV-A24 Joseph, and CV-A21 Coe were obtained from the National Institute of Public Health in Bilthoven, The Netherlands. RV-B14 was obtained from Joachim Seipelt, Medical University of Vienna, Vienna. CV-B3 was obtained by transfecting in vitro-transcribed RNA derived from full-length infectious clone p53CB3/T7 (Nancy).

Sequencing of CV-A24 Strains. CV-A24 isolate 73-17674 was obtained from the National Institute of Public Health in Bilthoven. This strain was isolated from a feces sample collected in 1973 by passaging twice in human diploid fibroblasts (Gabi) and once in HeLa-R19 cells. VP1 sequences of CV-A24 73-17674 and CV-A24v strains 110387 and 110389 were determined by PCR amplification of VP1 from cDNA, followed by Sanger sequencing.

Chemicals and Reagents. Soluble concatemerized VLDL-R (MBP-V33333) and monoclonal mouse anti-ICAM-1 (supersup) were gifts from Dieter Blaas, Medical University of Vienna, Vienna. ICAM-1 D1-D2 was prepared as described previously (3). Monoclonal mouse anti-PSGL-1 (clone KPL-1) was obtained from BD Biosciences (556052). Monoclonal mouse anti-integrin α2 (VLA-2 subunit α) (clone AA10) and monoclonal mouse anti-CAR (clone RmcB) were gifts from Jeffrey Bergelson, University of Pennsylvania, Philadelphia. Anti-PVR (NAEZ 8) and anti-integrin αvβ3 (NAGK4) were gifts from Merja Roivainen, National Institute for Health and Welfare, Helsinki. Polyclonal rabbit α-DAF was obtained from David John Evans, University of St Andrews, St Andrews, UK. Soluble ICAM-1 ectodomain was obtained from R&D systems (ADP4; recombinant human ICAM-1/CD54). Soluble CAR-D1 was obtained from Paul Freimuth, Brookhaven National Laboratory, Upton, NY. NA was obtained from Roche: *A. ureafaciens* (10269611001) or *V. cholera* (11080725001).

Cryo-EM Image Processing. Image processing was carried out using the RELION 2.0 pipeline (4, 5). Drift-corrected averages of each movie were created using MOTIONCOR2 (6) and the contrast transfer function (CTF) of each was determined using gCTF (7); any images showing signs of significant astigmatism were discarded. Initially, 896 particles were manually picked and classified using reference-free 2D classification. The resulting 2D class average views were used as templates for automated particle picking in RELION. Automated particle picking on lacey carbon grids resulted in a large number of boxes picked on the edges of holes in the carbon film. To remove such "junk" particles from the dataset, 2D classification in RELION was used with CTF amplitude correction only performed from the first peak of each CTF onward. Particles were further classified using several rounds of both reference-free 2D classification and 3D classification. After each round, the best classes/class was taken to the next step of classification. Postprocessing was employed to appropriately mask the model, estimate and correct for the B-factor of the maps. The final resolution of 3.9 Å was determined using the "gold standard" Fourier shell correlation (FSC = 0.143) criterion. Local resolution was estimated in RELION 2.0.

Model Building and Refinement. A preliminary model was generated by rigid body fitting the VP1-3 chains from the X-ray structure of CV-A24v (8) (PDB ID code 4Q4W) and ICAM-1 (Kilifi) D1 domain (9) (PDB ID code 1Z7Z) into the EM density map using UCSF Chimera (10). The model was then manually fitted in coot using the real space refinement tool (11). The resulting model was then symmetrized in Chimera to generate the capsid and subject to refinement in Phenix (12). Iterative rounds of manual fitting in Coot and refinement in Phenix were carried out to improve nonideal rotamers, bond angles, and Ramachandran outliers. The asymmetric unit was assessed for quality using MolProbity (13) and the model statistics for the refined capsid–ICAM-1 D1 complex were obtained from Phenix (Table S1). Interactions between ICAM-1 D1 and VP1-3 were analyzed using PDBePISA (14) and the roadmap projection of the CV-A24v surface was generated using RIVEM (15). The electrostatic surface potential of CV-A24v and ICAM-1 D1 were generated using the PDB2PQR server (16). Figures were generated using Chimera and Pymol.

Generation of Knockout Cells. The CRISPR/Cas9 was used to knock out ICAM-1 in HeLa, HAP1, HAP1 *CMAS*^{KO} and HCE cells by excision of the 1,489-nt region indicated in Fig. S1*C*. ICAM-1–specific gRNA sequences targeting exons 3 and 7 were introduced into pCRISPR-hCas9-2xgRNA-Puro as described previously (17). One day after transfection with this construct, cells were selected with puromycin (2 mg/mL) for 2 d, expanded, and subcloned. Individual subclones were genotyped by PCR amplification of gRNA target sites and subsequently sequenced.

Construction of CV-A24v 110390 Infectious cDNA Clones. The 5′ and 3′ halves of the CV-A24v 110390 genome were amplified separately and combined using an internal BstXI restriction site. Subsequently, the complete genome was cloned into XmaI and SalI sites of pRib-CB3-Luc (18) from which the CB3-Luc region was deleted using the same enzymes, to yield pRib-CVA24v-110390. Sequence analysis confirmed that the sequences of the viral cDNAs were identical to that of the viral RNA. pRib-CVA24v-110390-Y1250F, containing substitution VP1 Tyr^{250} Phe, was made using the Q5 site-directed mutagenesis kit (New England Biolabs). Infectious virus was generated by transfection of plasmids into Huh7/Lunet/T7 cells, which initiate transcription from the T7 promotor lying upstream of the viral cDNA. Virus was harvested, followed by verification of the genomic sequence.

1. Sosne G, Hafeez S, Greenberry AL, 2nd, Kurpakus-Wheater M (2002) Thymosin beta4 promotes human conjunctival epithelial cell migration. *Curr Eye Res* 24: 268–273.
2. Ghazali O, et al. (2003) An outbreak of acute haemorrhagic conjunctivitis in Melaka, Malaysia. *Singapore Med J* 44:511–516.
3. Casasnovas JM, Stehle T, Liu J-H, Wang J-H, Springer TA (1998) A dimeric crystal structure for the N-terminal two domains of intercellular adhesion molecule-1. *Proc Natl Acad Sci USA* 95:4134–4139.
4. Scheres SHW (2012) RELION: Implementation of a Bayesian approach to cryo-EM structure determination. *J Struct Biol* 180:519–530.
5. Kimanius D, Forsberg BO, Scheres SHW, Lindahl E (2016) Accelerated cryo-EM structure determination with parallelisation using GPUs in RELION-2. *eLife* 5:1–21.
6. Zheng SQ, et al. (2017) MotionCor2: Anisotropic correction of beam-induced motion for improved cryo-electron microscopy. *Nat Methods* 14:331–332.
7. Zhang K (2016) Gctf: Real-time CTF determination and correction. *J Struct Biol* 193: 1–12.
8. Zocher G, et al. (2014) A sialic acid binding site in a human picornavirus. *PLoS Pathog* 10:e1004401.
9. Xiao C, et al. (2005) The crystal structure of coxsackievirus A21 and its interaction with ICAM-1. *Structure* 13:1019–1033.
10. Pettersen EF, et al. (2004) UCSF Chimera–A visualization system for exploratory research and analysis. *J Comput Chem* 25:1605–1612.
11. Emsley P, Lohkamp B, Scott WG, Cowtan K (2010) Features and development of Coot. *Acta Crystallogr D Biol Crystallogr* 66:486–501.
12. Headd JJ, et al. (2012) Use of knowledge-based restraints in phenix.refine to improve macromolecular refinement at low resolution. *Acta Crystallogr D Biol Crystallogr* 68:381–390.
13. Chen VB, et al. (2010) MolProbity: All-atom structure validation for macromolecular crystallography. *Acta Crystallogr D Biol Crystallogr* 66:12–21.
14. Krissinel E, Henrick K (2007) Inference of macromolecular assemblies from crystalline state. *J Mol Biol* 372:774–797.
15. Xiao C, Rossmann MG (2007) Interpretation of electron density with stereographic roadmap projections. *J Struct Biol* 158:182–187.
16. Dolinsky TJ, Nielsen JE, McCammon JA, Baker NA (2004) PDB2PQR: An automated pipeline for the setup of Poisson-Boltzmann electrostatics calculations. *Nucleic Acids Res* 32:W665–W667.
17. Langereis MA, Rabouw HH, Holwerda M, Visser LJ, van Kuppeveld FJM (2015) Knockout of cGAS and STING rescues virus infection of plasmid DNA-transfected cells. *J Virol* 89:11169–11173.
18. Lanke KHW, et al. (2009) GBF1, a guanine nucleotide exchange factor for Arf, is crucial for coxsackievirus B3 RNA replication. *J Virol* 83:11940–11949.

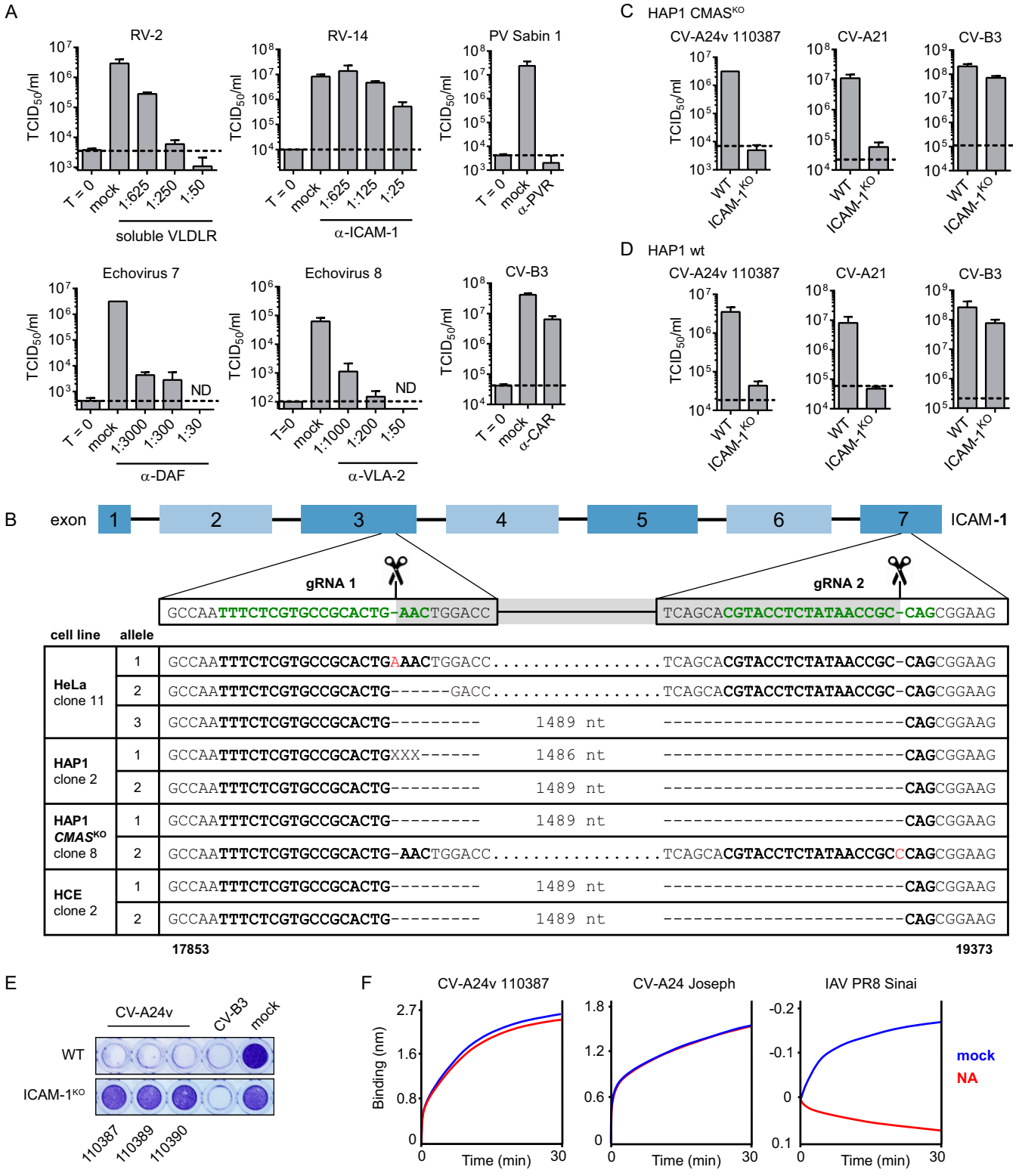

Fig. S1. (*A*) Receptor-specific antibodies and soluble VLDL-R inhibit infection of control viruses. HeLa-R19 cells (RV-A2 and RV-B14), HAP1 CMAS^{KO} cells (PV, echovirus 8 and CV-B3), or RD cells (echovirus 7) were infected and yields of infectious virus were determined after a single replication cycle. PV, poliovirus; RV-2, rhinovirus A2; RV-14, rhinovirus B14. (*B*) Genomic sequences of ICAM1^{KO} cells lines. Each line represents the *ICAM-1* sequence from nucleotides 17,853–19,373 of one chromosome in the indicated clones. The sequence corresponding to guide RNA 1 is marked in bold on the left side of the sequence, and that corresponding to guide RNA 2 is marked in bold on the right side. Insertions are marked in red and dashed lines indicate gaps in the sequence, showing the number of nucleotides for large deletions. Dots represent parts of the sequence that are not shown. (*C* and *D*) HAP1 CMAS^{KO} cells (*C*) or HAP1 WT cells (*D*) in which ICAM-1 was knocked out (ICAM-1^{KO}) were infected and yields of infectious virus were measured after a single replication cycle. Dashed lines (*A*, *C*, and *D*) represent virus input levels (T = 0). Error bars (*A*, *C*, and *D*) represent the mean ± SEM of three biological replicates. (*E*) HCE cells were infected with various CV-A24v clinical isolates or CV-B3, followed by crystal violet staining of surviving cells. (*F*) Biolayer interferometry analysis of virus binding to mock- or NA-treated ICAM-1. Influenza A virus Puerto Rico/8/34/Mount Sinai (IAV PR8 Sinai) was used as a positive control for NA treatment.

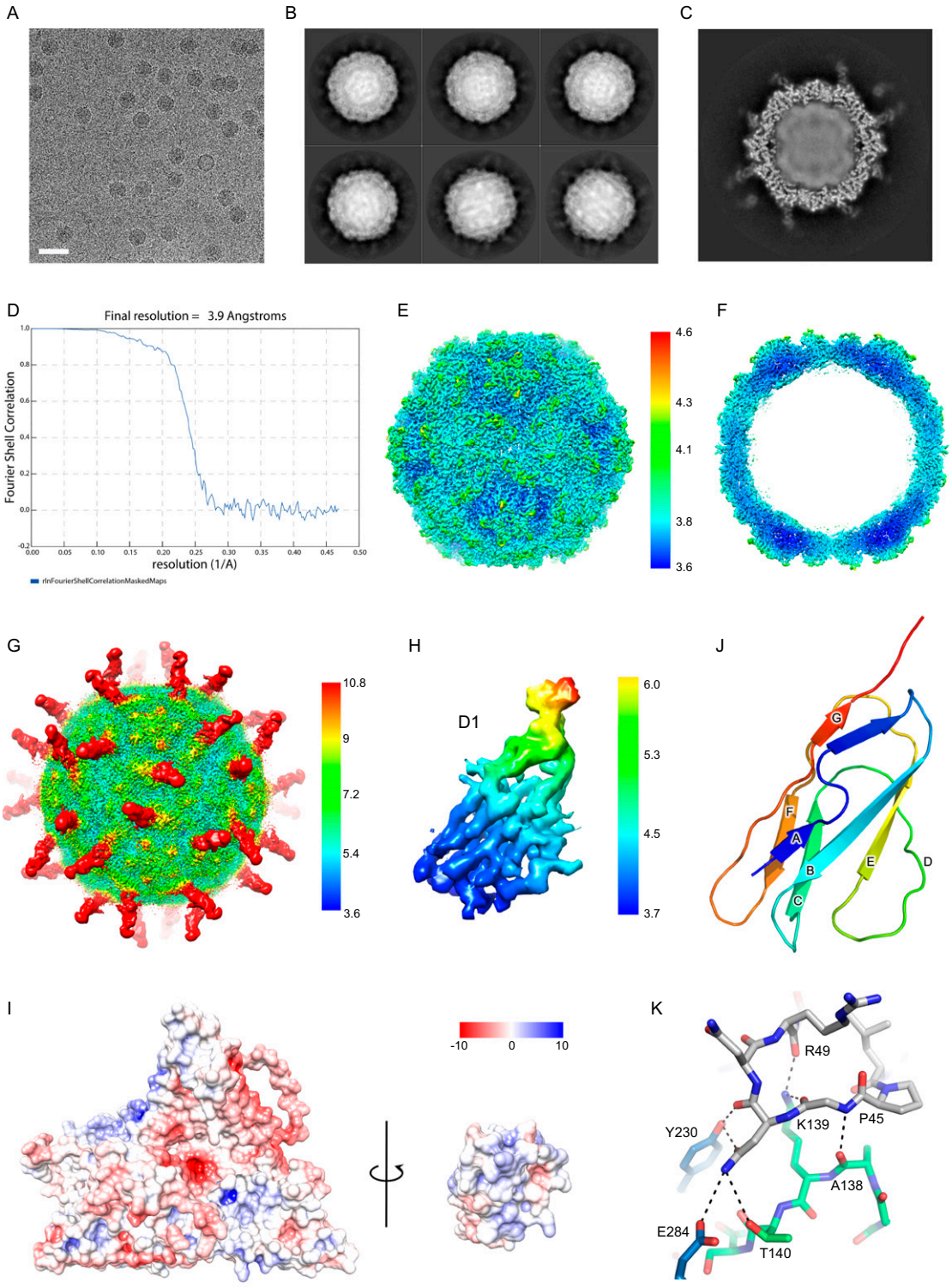

Fig. S2. (*A*) Typical micrograph of CV-A24v in complex with ICAM1-D1D2 (Scale bar, 50 nm). (*B*) Representative 2D class averages generated in RELION. (*C*) Central slice through 3D reconstruction generated in RELION. (*D*) A plot of the Fourier shell coefficient (FSC). Based on the 0.143 criterion for the gold standard comparison of two independent datasets, the resolution of the reconstruction is 3.9 Å. (*E*) The cryo-EM reconstruction of CV-A24v in complex with ICAM-1 (D1D2) viewed down the icosahedral twofold axis and colored according to local resolution (3.6σ). (*F*) A 40-Å slab through the center of the map shown in *A*. (*G*) The cryo-EM reconstruction of CV-A24v in complex with ICAM-1 (D1D2) viewed down the icosahedral twofold axis and colored according to local resolution (0.6σ). (*H*) Segmented D1 domain from ICAM-1 colored according to local resolution. (*I*) Electrostatic surface representation of the CV-A24v capsid (*Left*) and interacting face of ICAM-1 D1 (*Right*) colored red to blue ranging from most negative (−10 kT/e) to most positive (+10 kT/e). Neutral surface is colored white. (*J*) Ribbon diagram of ICAM-1 D1 monomer in chainbow coloring with secondary structure labeled as described previously (9). (*K*) Hydrogen bonding network between the DE loop of D1 (gray), VP2 (green), and VP1 (blue) with hydrogen bonds shown as dashed black lines. Oxygen and nitrogen atoms are colored red and blue, respectively.

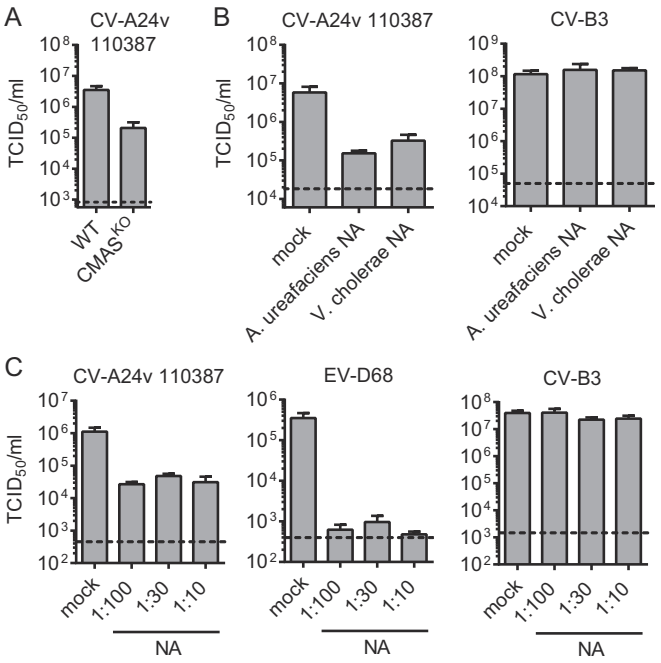

Fig. S3. Depletion of Sia partially inhibits CV-A24v infection. (*A*) Sia-deficient HAP1 CMAS^{KO} cells were infected with CV-A24v 110387 on ice and yields of infectious virus were determined after a single replication cycle. (*B*) HCE cells were treated with 1:10 diluted *A. ureafaciens* NA or *V. cholerae* NA, infected on ice, and yields of infectious virus were determined after a single replication cycle. (*C*) HAP1 cells were treated with various concentrations of *A. urefaciens* NA, infected on ice, and yields of infectious virus were determined after a single replication cycle. Virus production of the strictly Sia-dependent EV-D68 is reduced completely to input levels by Sia depletion, CV-A24v is partially inhibited, and CV-B3 is unaffected. Dashed lines (*A*–*C*) represent virus input levels (T = 0). Error bars (*A*–*C*) represent the mean ± SEM of three biological replicates.

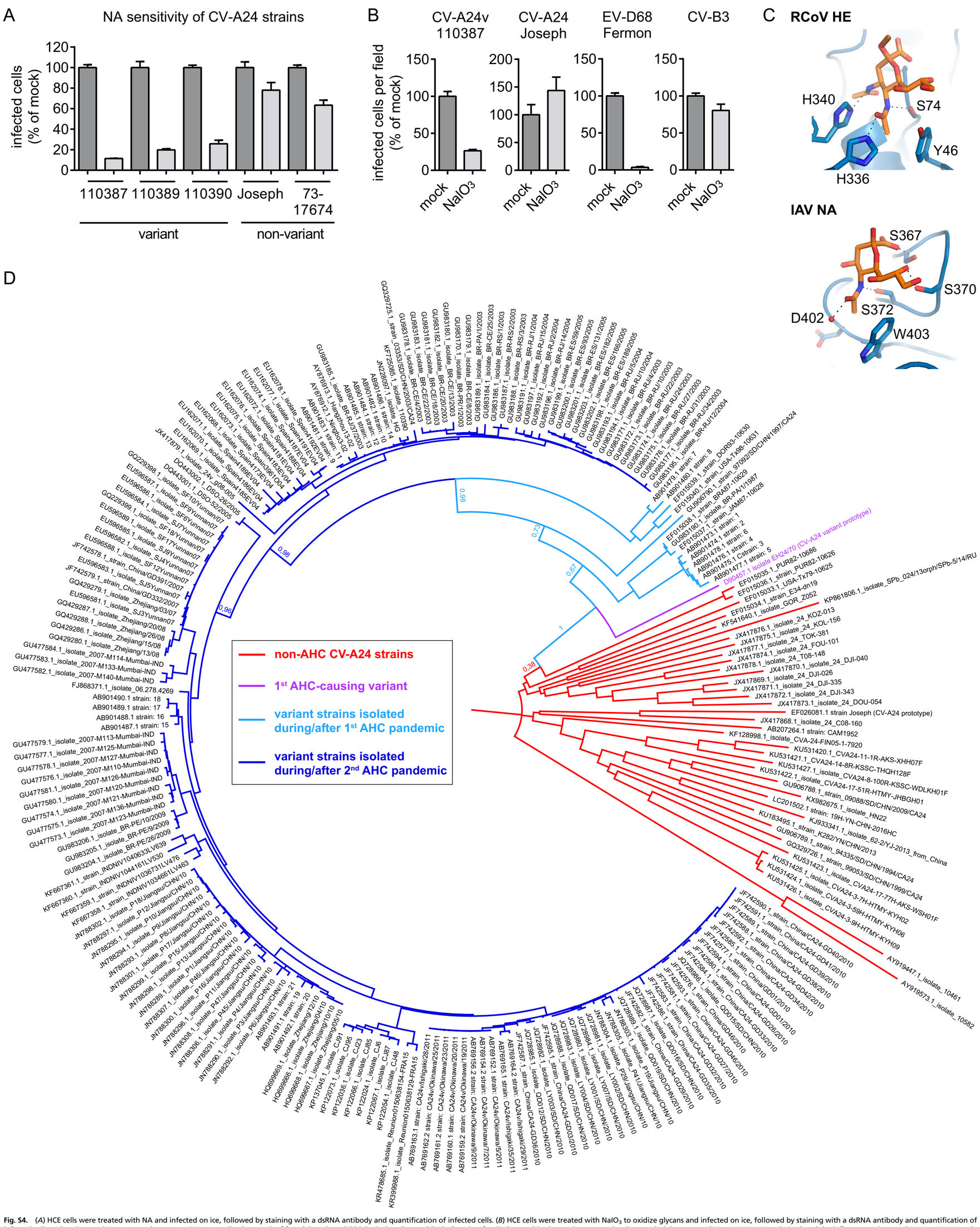

Fig. S4. (*A*) HCE cells were treated with NA and infected on ice, followed by staining with a dsRNA antibody and quantification of infected cells. (*B*) HCE cells were treated with $NaIO_3$ to oxidize glycans and infected on ice, followed by staining with a dsRNA antibody and quantification of infected cells. Values in *A* and *B* represent the mean ± SEM normalized to mock of four (*A*) or three (*B*) biological replicates. (*C*) Binding sites for Sia (orange) in the murine coronavirus hemagglutinin-esterase (RCoV HE; PBD ID code 5JIL) and the influenza A virus NA (IAV NA; PBD ID code 1MWE), showing that the 5-*N*-acyl group of Sia is stabilized by two hydrogen bonds (dashed lines). Red spheres represent water molecules. Oxygen and nitrogen atoms are colored red and blue, respectively. (*D*) Neighbor-joining tree of all complete CV-A24 VP1 nucleotide sequences available on GenBank on January 1, 2017. The indicated bootstrap values were calculated for 1,000 replicates.

Table S1. Cryo-EM data statistics

Data collection	
Microscope	FEI Titan Krios
Camera	Falcon III
Voltage	300 keV
Pixel size	1.065 Å
Total dose	60 e-/Å^2
No. of frames	40
Defocus range	0.5–3 μm
Micrographs	2,652
Acquisition software	FEI EPU
Image processing	
Motion correction	MotionCor2
CTF estimation	Gctf
Reconstruction	
Software	RELION 2.0
Particles contributed	26,311
B-factor	−257
Resolution (FSC 0.143)	3.9 Å
Model building and refinement	
Model refinement software	Phenix real space
Map CC (whole unit cell)	0.75
Map CC (all atoms)	0.87
Rmsd bond length	0.01
Rmsd bond angles	0.87
Ramachandran preferred	94.09%
Ramachandran allowed	5.91%
Ramachandran outlier	0.00%
Rotamer outliers	0.40%
C-beta deviations	0
All-atom clash score	4.37

Table S2. Loss of amino acid diversity at VP1 sites with high amino acid polymorphism among nonvariant CV-A24 strains

	Amino acid residue	
Location	Nonvariant	Variant
4	D/E	E
11	S/N	S/T
22	Q/N/S	Q
25	L/E/P	L/H/P
31	A/P/T/V	P
32	S/A	S/L/P
33	T/S	T
38	S/T	S
56	V/I	V/I
99	T/S/N/Q	T
100	E/D/T/L	D/E
101	A/E/S/T/D/G/R	A
104	K/R	K
109	T/R/I/V	T
140	V/I	I
149	T/S/A	T
168	Q/R/K/I	R
170	T/N/A	T
196	M/I/L	M/I
221	D/G	D
223	T/A/D/V	T
224	T/A	V
259	V/I	I
284	E/D	E
291	D/G/S/T	D
292	S/A/T	S
300	A/T/N/D/S/K	E
301	S/N/D/K/T	N/D

All strains shown in Fig. S4*D* were used.

Table S3. Amino acid composition of CV-A24 capsid sites interacting with ICAM-1

			Amino acid residue		
Type of interaction	Protein	Location	Nonvariant	First AHC-causing variant (EH24/70)	Variant
Salt bridges	VP1	168	Q/R/K/I	R	R
		225	D	D	D
		228	D	D	D
		238	D	D	D
	VP3	181	D	D	D
Hydrogen bonds	VP1	223	T/A/D/V	T	T
		224	T/A	V	V
		230	F/Y	Y	Y
		284	E/D	E	E
	VP2	138	A/N/V	A	A
		139	K	K	K
		140	T	T	T
		142	Y	Y	Y
	VP3	182	D	D	D

For analysis of VP1, all strains shown in Fig. S4*D* were used. Analysis of VP2 and VP3 was based on a subset of these strains.